

AERODYNAMIC INVESTIGATIONS ON A GENERIC FAN-IN-WING CONFIGURATION

N. Thouault*, C. Gologan, C. Breitsamter* and N.A. Adams***

***Institute of Aerodynamics, Technische Universität München**

**** Bauhaus Luftfahrt e.V.**

Boltzmannstrasse 15, D-85748 Garching, Germany

Keywords: *Fan-in-wing, cross-flow, sliding mesh, unsteady RANS, code validation*

Abstract

The present investigation focuses on the comparison of Computational Fluid Dynamics (CFD) results with experimental data for a generic fan-in-wing configuration. The objective is to reproduce a Short-Take-Off and Landing (STOL) or a transition-flight situation without ground effect. A rotating fan is placed in the wing plane, inside of the wing rear part close to the root section. The obtained experimental data include Particle Image Velocimetry (PIV), force measurements, surface pressure measurements and wool-tufts visualization. A structured mesh of the entire configuration with minimum geometrical simplifications is used to perform Unsteady Reynolds-Averaged Navier Stokes (URANS) computations. The area surrounding the rotor blades is set up as sliding mesh to simulate the rotation using the ANSYS CFX commercial software. The fan-in-wing configuration features a complex flow field. The generated cross-flow notably affects the fan efficiency. The interaction of the incoming flow with the transverse jet influences considerably the wing performance. Time-averaged URANS results over one fan revolution show a good agreement with the experimental data. A profile imperfection of the wind tunnel model affects lightly the wing behavior at high angle of attack. The major turbulence phenomena are well predicted by the simulation.

1 Introduction

The fan-in-wing concept was originally proposed to allow for S/VTOL (Short/Vertical Take Off and Landing) missions. It was implemented in the jet powered experimental aircraft Ryan GE XV-5 in the 1960's. Many experimental investigations on fan-in-wing configurations can be found in NASA technical notes. Most of them are related to the development of the Ryan GE XV-5 experimental aircraft. The surveys of Refs. 1 and 2 provide a good overview of all the investigations conducted and summarizes the main results. These studies point out the complexity of the flow due to the fan installed in the wing. For instance, the inflow distortion and the back-pressure at the fan nozzle are critical parameters in this cross-flow problem [1]. The interaction of the jet with the freestream is also a major issue. The flow exiting the fan nozzle is similar as a jet-in-cross-flow problem. The jet-in-cross-flow has received considerable attention during the last years particularly concerning its application in S/VTOL aircraft. A jet exhausting an aircraft out-of-ground effect generates a complex flow field and features several characteristics (e.g.: jet swept back by the freestream following a curved path, jet blockage and entrainment) [3]. Four major vortical structures have been established in comprehensive jet-in-cross-flow analysis: (a) horse shoe vortices formed upstream of the jet exit and wrapping around the jet column ([4, 5, 6]), (b) wake vortices [5], (c) jet shear layer vortices formed also upstream of the jet [6], (d) a pair of counter-rotating vortices

located downstream of the jet exit [7]. Unsteady sliding mesh simulations of an embedded cross flow fan into a thick wing have recently been performed [8]. This two-dimensional analysis differs from the flow topology of the proposed fan-in-wing configuration. The present study investigates a three-dimensional configuration with a fan rotating in the plane of a wing (Fig. 1). A fan composed of a rotor and a stator is placed at the rear part of the wing. The fan ingests a part of the incoming flow boundary layer. After compression, the air is ejected through the nozzle therefore creating a jet-in-cross-flow.

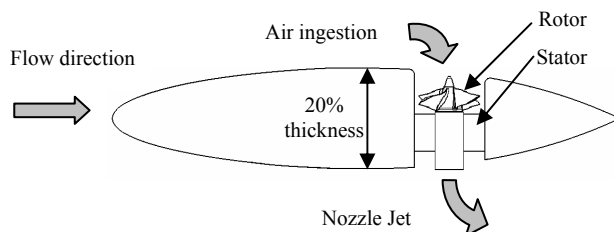


Fig. 1 Schematic view of the experimental setup.

A wide range of experimental results has been gathered in a previous study [9] including flow field mapping using Particle Image Velocimetry (PIV), forces and surface pressure measurements and wool tufts visualization. The present investigation concentrates on the comparison of the numerical results with experimental data. In addition, a discussion concerning the fan efficiency is given.

2 Experimental technique

In this section, wind tunnel model and experiments are described. Selected results of forces measurements are presented and give an overview of the model behavior.

2.1 Wind tunnel model

The model airfoil is a NACA 16-020 with 20% thickness. It provides enough space to insert two fans inside the wing. The semi-span wing model has an aspect ratio of 2.3, a semi-span area of 0.683 m², a taper ratio of 0.71 and a 0° sweep of the 50% root chord line. The model is designed to investigate several generic fan-in-wing configurations: (i) the closed wing without fan

set as reference, (ii) one single fan installed either at the rear (Fig. 2) or in the front part of the wing and (iii) two fans placed symmetrically with respect to the half chord. The geometry modeled in the numerical simulation is the one presented in Fig. 2 for a single fan at the wing rear part. The rear fan axis position is located $\frac{2}{3}$ of the root chord, c , and at 0.12 wing span, s , from the root chord. The fan has a diameter 13% of c . On the wing upper side the lip radius to diameter was set as 8 % (Fig. 3b). The model is installed on a peniche to raise the wing out of the wind tunnel wall boundary layer.

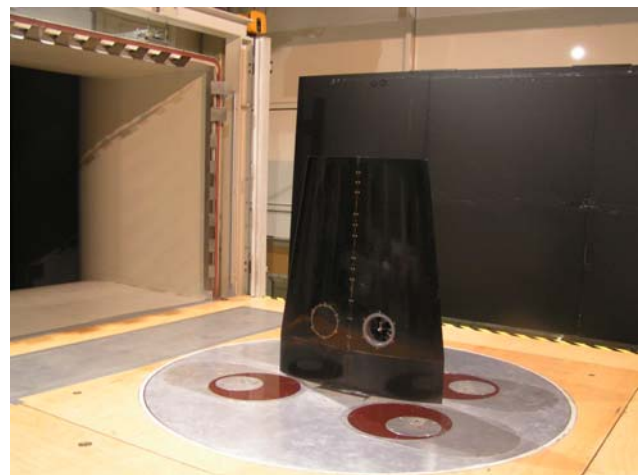


Fig. 2 Model in wind tunnel.

The fan used during the experiment is originally employed for radio/controlled purpose. It fan is composed of two stages, a four-blade rotor and four-blade stator. The engine is located inside the stator and therefore gives a realistic configuration with no external device around the wing. Only the cables to provide power and to measure the engine temperature are a cause of disturbance.

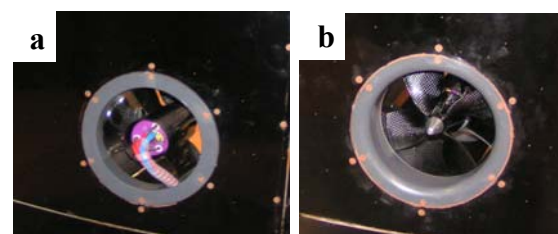


Fig. 3 Zoom a. on the nozzle, b. on the inlet radius.

These cables are located behind one stator blade trailing edge (Fig 3a) to minimize their influence.

2.2 Wind tunnel data

The results presented in this section concern the configuration in which a single fan is set at the wing rear part (Fig. 2).

A variety of experimental techniques were used to provide a reliable database for simulation validation. Four different types of tests have been conducted in the wind tunnel campaign: wool-tufts flow visualization, flow-field mapping using Stereo-PIV near the trailing edge, force measurements and surface static pressure measurements. For the force measurements, the angle-of-attack polars were performed between $\alpha = -10^\circ$ to $\alpha = 20^\circ$, out of the stalled region. PIV measurements were only carried out at a specific operating condition detailed in section 4.4. Three different freestream velocities, V_∞ , were investigated: 30 m/s, 40 m/s and 50 m/s corresponding to a Reynolds number based on the root chord of $Re_c = 1.5 \times 10^6$, $Re_c = 2 \times 10^6$, $Re_c = 2.5 \times 10^6$ respectively. Three different fan rotation speeds were investigated: $N = 21,000$ rpm, 23,700 rpm and 26,500 rpm. The ratio of the freestream velocity over the fan rotation speed at the tip defines the tip-speed ratio, μ , as proposed in [10]. It characterizes the freestream capability to deflect the nozzle jet. A strong jet deflection (high μ) induces less pressure drag but also less lift whereas a weak jet deflection (low μ) results in higher drag and higher lift coefficient [9]. The jet created by the fan at the rear position induces a blocking of the freestream. The flow exiting the nozzle acts as a jet flap therefore increasing the circulation and the lift coefficient (Fig. 4a). The offset between the two lift polars is partly due to the fan thrust and partly to the induced lift generated by this jet flap effect. The cross-flow generated by the fan provokes a significant increase of the drag coefficient compared to the reference case without fan. The relative increase in drag tends to be higher at high angle of attack (Fig. 4b). Considering the pitching moment (with respect to the quarter chord), the fan inside the wing induces a nose down pitching moment (Fig. 4c) compared to the reference case. Chordwise pressure measurements presented in the last section

corroborates the previous statements. Further experimental results are shown in section 4.

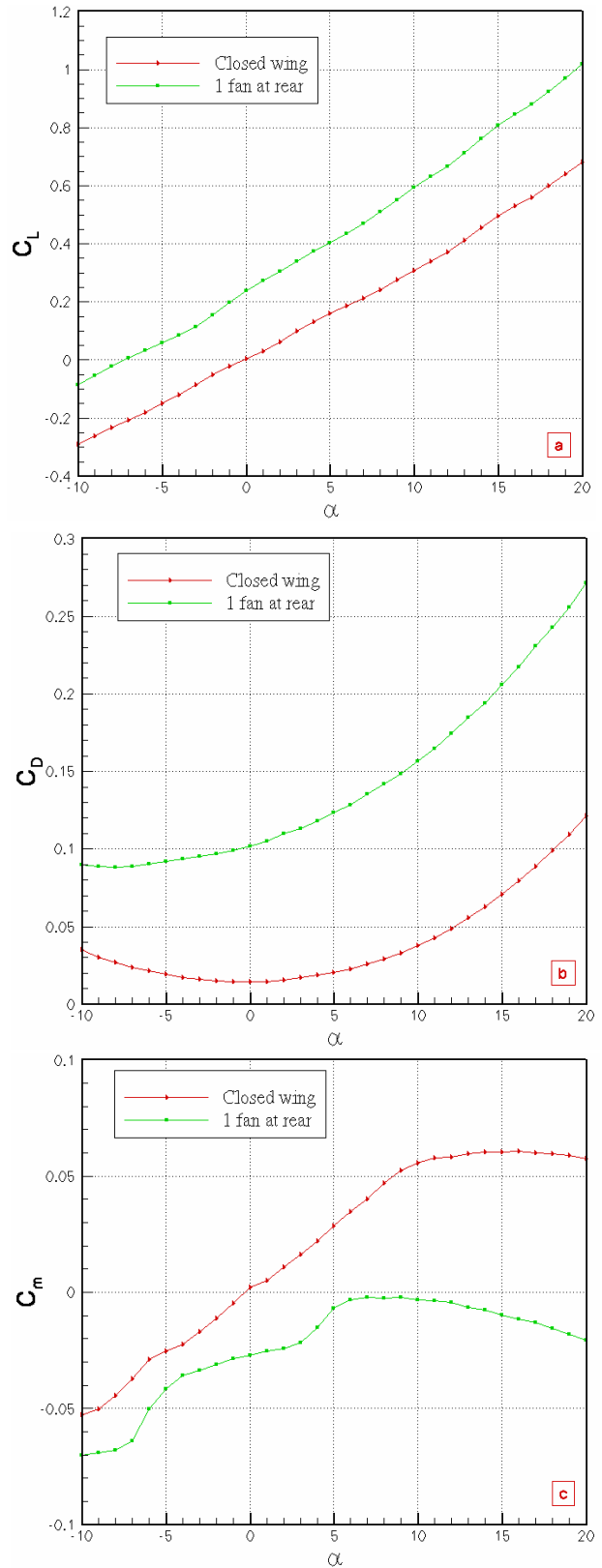


Fig. 4 a. Lift coefficient, b. Drag coefficient, c. Pitching moment coefficient (with respect to $c/4$) for $V_\infty = 30$ m/s and $N = 21,000$ rpm ($\mu = 0.227$).

3 CFD simulations

ANSYS CFX flow simulation software is used to perform CFD simulations of this fan-in-wing configuration. A second order discretization of the convective terms is used throughout all calculations. The $k-\omega$ SST model from Menter is used for all computations [11]. To simulate the fan rotation during steady calculations, a reference frame transformation between the area surrounding the blades and the rest of the computational domain is done by frozen-rotor interfaces [12]. For the unsteady calculation, the area surrounding the blades is designated as sliding mesh. The residuals are less than 10^{-5} for continuity terms and less than 10^{-4} for all other residuals (heat transfer, momentum and turbulence quantities). The total energy model is used to account for compressibility effects, especially significant at the rotor blade tip and on the inlet radius. The maximum Mach number in this area approaches $M = 0.7$. For calculation of the wing without fan, the incompressible solver is used ($M < 0.15$).

The initial data for the unsteady run are obtained in performing a steady calculation. Unsteady simulations require a proper setting of the time step. It is chosen appropriately referring to the mesh. A complete revolution is made in 286 time steps for the baseline mesh. All the unsteady results presented in this paper represent time-averaged data over one fan rotor revolution. A number of 24 CPUs on a 512 nodes Altix cluster is used, with a computational time of about 2 days for the steady simulation and 6 days for the unsteady case, corresponding approximately to 5 complete rotor revolutions for the baseline mesh. A monitor point showing the total pressure in the rotating domain is set. After 5 revolutions the variation of the total pressure at this point is periodic.

3.1 Pre-processing

3.1.1 Mesh topology

A multiblock structured mesh is generated around the geometry. The rotor blade geometry itself is highly twisted and requires particular attention when creating mesh blocks. ANSYS ICEM CFD is used for this purpose. This type

of mesh has been selected to obtain more accurate results especially in the near wall region. Special attention has been given to the nearest mesh node in the viscous sublayer for a good prediction of the separated regions on the wing and on the fan blades. A value of $y_+ < 1$ is achieved for the most part of the attached flow on the wing and fan blade surfaces. On the inlet radius, the wing and the rotor blade tips, the value of y_+ remains below 4. Overall, 939 blocks were created. This number of blocks is necessary to avoid negative volumes and obtain a relatively good mesh quality in terms of orthogonality, minimum angle and aspect ratio. The geometry requires an unconventional blocking strategy. An O-grid topology is set around each fan blade and around the wing. The overall computational topology is a C-H topology, commonly used for external aerodynamic numerical simulation. As usually done, 10 chords were taken in each direction from the wing to create the computational domain. Special care has been taken to create a continuous blocking around all the geometry to avoid different surface meshes between blocks inducing numerical diffusion. To be used in CFX the multiblock mesh is converted to an unstructured mesh. The surface mesh on the rotor blades and hub is shown in Fig. 5.

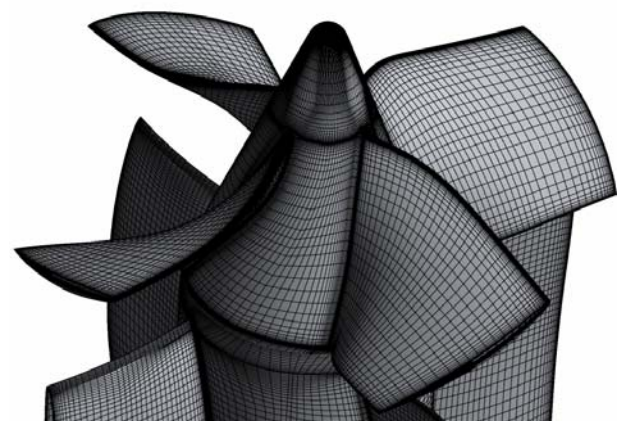


Fig. 5 Surface mesh on the rotor blades and hub.

Geometrical simplifications cannot be avoided considering the complexity of the geometry. The influence of the wires providing power to the engine is neglected in the numerical simulation. Located behind one stator blade trailing edge (Fig. 3a), they are assumed to have only a small influence on the overall results and

therefore are not modeled. The fan geometry is simplified to create a suitable blocking around the geometry. The gaps between the rotor and stator and the holes are removed. The rotor blade filets are also neglected. Thus, the blade geometry in the hub vicinity is extrapolated. Despite these changes, the rest of the geometry is precisely modeled, including the region between the rotor blade tip and the shroud to capture secondary flows.

3.1.2 Simulation setup

For the wing without fan, a symmetry condition can be set on the plane of the wing root chord. Due to the jet interaction exiting the fan nozzle, a symmetry condition (at this position) is not used. Therefore, the peniche is included in the computational domain for all the simulations. A free slip wall boundary condition is then applied to model the wind tunnel floor. The effect of the wind tunnel floor is assumed to have a negligible influence on the wing.

The computational domain was divided into two parts: a rotating domain around the rotor and a stationary domain containing the rest. The connection between these two domains is made by interfaces. For the steady simulation, both interfaces are specified as frozen rotor [12].

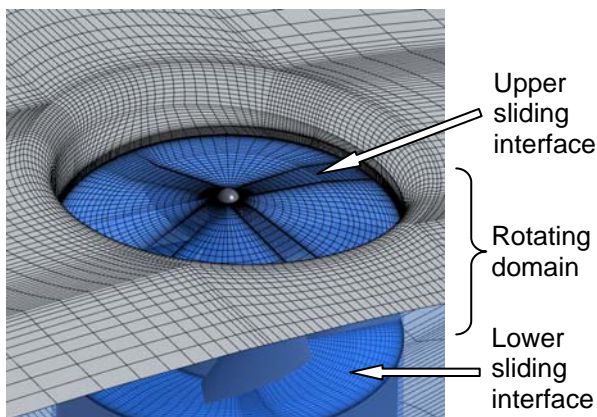


Fig. 6 Sliding interfaces position, inlet radius and wing upper side mesh.

In this case, the results depend on the initial position of the blade and do not describe accurately the rotor/stator interaction. The area surrounding the rotor blades is modeled as a moving reference frame zone.

For the unsteady simulations, the rotor domain is rotating using a sliding mesh. The interaction

between the rotor and stator is thus taken into account and therefore provide a more realistic model. Sliding interfaces separate the rotating domain from the stationary domain (Fig. 6).

3.1.3 Grid-dependence study

For the fan-in-wing configuration, the steady calculation provides a very good initial solution for the external aerodynamics. The mass flow rate and total pressure rise are comparable to the unsteady results. The steady solution was obtained when all the forces acting on the body slightly oscillate around a mean value. The grid study is here presented considering mean value results. A grid-dependence study for the time-averaged unsteady calculation is in progress.

Three different mesh densities were tested: a coarse grid of 2.6 million cells, a medium grid of 4 million cells and a fine grid of 9 million cells. The forces predicted with the finer mesh are closer to the experimental results. According to Table 1, the comparison of the steady results shows only a small difference between the medium and fine grid. Therefore, all the calculations are performed with the 4 million nodes medium grid. The thrust coefficient, C_T , is defined as the ratio of the fan thrust over the product of the planform area times the freestream dynamic pressure.

	Coarse grid	Medium grid	Fine grid
C_L	0.258	0.266	0.268
C_D	0.093	0.094	0.095
C_m	-0.035	-0.037	-0.039
C_T	0.036	0.037	0.037

Table 1. Comparison of aerodynamic coefficients for different grid levels at $V_\infty = 40$ m/s, $\alpha = 0^\circ$ and $N = 26$, 200 rpm ($\mu = 0.243$).

3.2 Closed wing without fan

The closed wing without fan is also simulated to provide insight of the wing flow field and to serve as reference. At $\alpha = 0^\circ$, separation occurs at the trailing edge at approximately 93% of the root chord. Angle-of-attack polars are given in section 2.2 for the lift, drag and pitching moment coefficient (Fig. 4). A mismatch is observed at high angle of attack (Table 2). The pressure measurements indicate an imperfection

in the wing airfoil at the leading and trailing edge. The geometry numerically simulated is perfectly symmetric and does not include this slight camber. Thus the separation prediction at the trailing edge differs slightly from the experiment resulting in an overestimation of the lift coefficient at high angle of attack. At $\alpha = 5^\circ$, the relative error in lift coefficient is about 6% and 16% at $\alpha = 10^\circ$. Drag and pitching-moment coefficients are in satisfying agreement with the experimental values. The analysis presented in the next section will focus on the case without angle of attack for which the airfoil asymmetry has a negligible effect.

		$\alpha = 0^\circ$	$\alpha = 5^\circ$	$\alpha = 10^\circ$
C_L	Num.	0.003	0.172	0.309
	Exp.	0.006	0.162	0.366
C_D	Num.	0.017	0.021	0.038
	Exp.	0.015	0.022	0.037
C_m	Num.	-0.001	0.028	0.033
	Exp.	0.002	0.029	0.046

Table 2 Closed wing aerodynamic coefficients at $V_\infty = 30$ m/s.

3.3 Unsteady results

All the results presented in this section refer to a freestream velocity of $V_\infty = 40$ m/s ($Re_c = 2 \times 10^6$), a fan rotation speed of $N = 26,200$ rpm (which corresponds to $\mu = 0.243$). The angle of attack is $\alpha = 0^\circ$ to isolate the fan contribution and the induced aerodynamic effects on the overall flow.

3.3.1. Flow visualization

Flow visualization is presented for a plane cutting the fan center. The results show that the main features encountered in a jet in transverse flow, listed in the introduction, are predicted by the simulation.

The adverse pressure gradient formed at the fan exit causes the wall boundary layer to separate and therefore create the horseshoe vortex (Fig. 7 (a)). The horseshoe vortex wraps around the jet column (Fig. 13). The incoming flow on the wing upper side is strongly entrained by the jet. Thus the flow remains attached at the trailing edge (b). As previously stated, the flow separates at about 93% of the chord for the closed wing without fan at $\alpha = 0^\circ$. The fan has

the capability to maintain attached flow at the wing trailing edge in a small region downstream of the inlet radius (Fig 13).

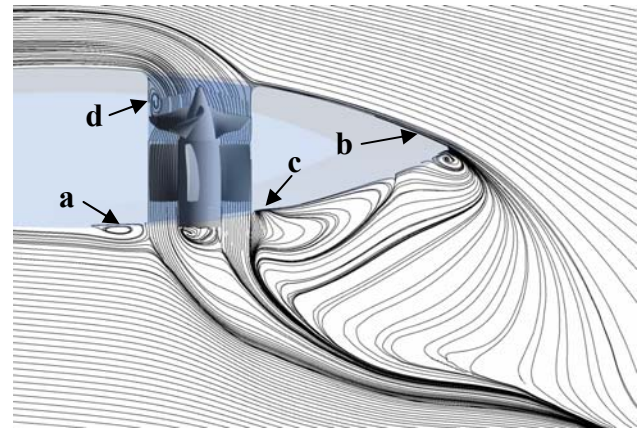


Fig. 7 Surface streamlines at 0.12 s from the wing root chord ($\alpha = 0^\circ$, $V_\infty = 40$ m/s, $N = 26,200$ rpm).

The existence of a saddle point on the leeward side of the jet is predicted by the simulation (c). The streamlines from this saddle point indicates a small flow region close to the wing surface following the streamwise direction. The recirculation area below the hub at the fan exit is also predicted by the simulation. On the wing upper side, the streamline visualization indicates the presence of two stagnation areas respectively located at the hub nose and on the inlet radius downstream of the fan. The flow separates at the inlet radius upstream of the fan. A further analysis of the separation bubble (d) occurring above the rotor blade as well as discussion on the pair of counter-rotating vortices is given in the next sections.

3.3.2 Inflow distortion

The abrupt deflection of the flow by the fan is causing a non uniform inflow velocity profile. The area upstream of the fan inlet features high velocities whereas downstream of the hub nose, a low velocity area is seen (Fig 8a). Separation occurs on the inlet radius therefore generating a recirculation area, with low Mach number in its core, above the rotor blades. The asymmetric (to the fan middle line) velocity distribution reveals an advancing and retreating condition on the rotor blades. Note that the fan rotational sense is counterclockwise as seen from above. The time-averaged pressure coefficient distribution on the wing and inlet radius depicts also retreating and advancing conditions and show that the pressure

distribution above the rotor blade is highly distorted (Fig. 8b).

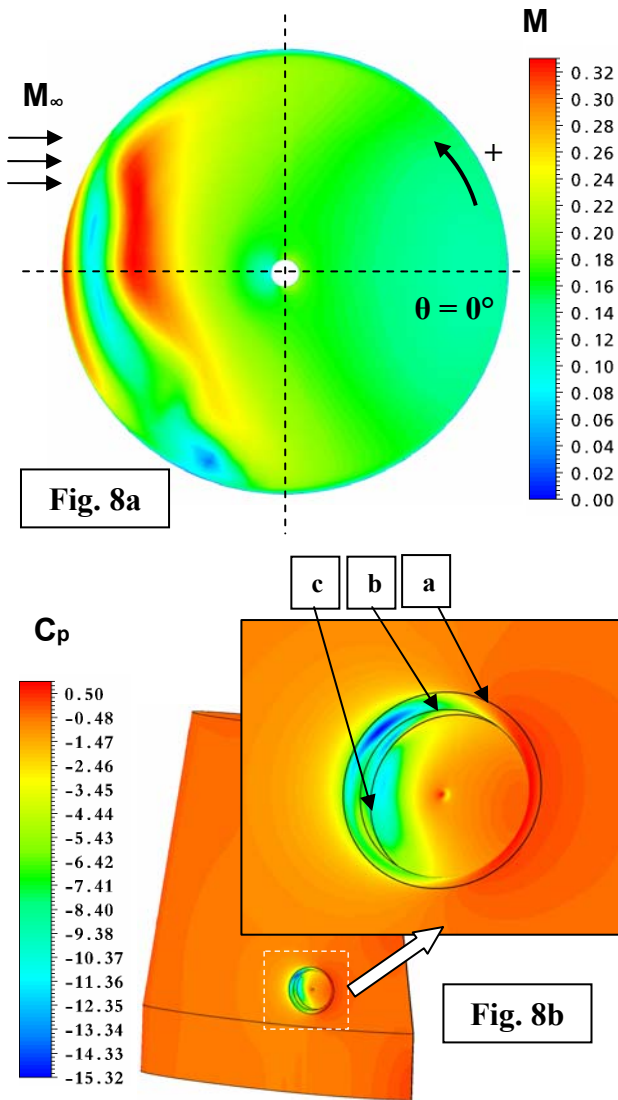


Fig. 8a

Fig. 8b

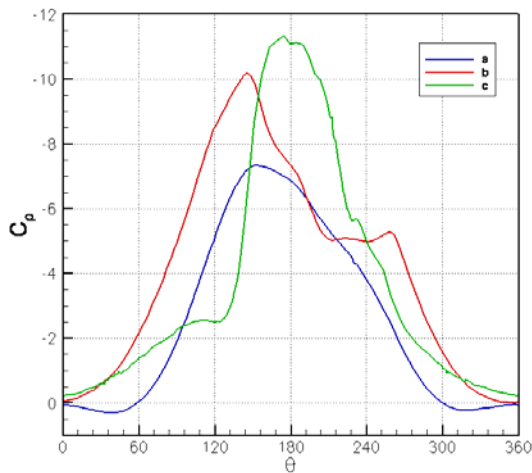


Fig. 8 c. Mach contour on the upper sliding interface
 b. Pressure coefficient contour on the wing and the sliding interface ($\mu = 0.243$).

This distortion is confirmed by the radial pressure distribution plotted below. The distortion is weak and almost symmetric to $\theta = 180^\circ$ on the radial pressure distribution (a), unlike distributions (b) and (c). As seen from the streamlines on Fig.7, the presence of stagnation areas on the hub nose and downstream of the fan on the inlet radius respectively is confirmed by the time averaged-pressure coefficient distribution.

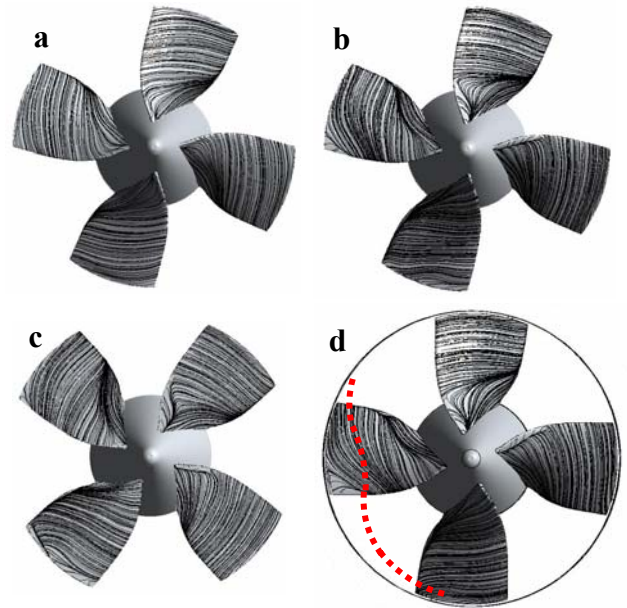


Fig. 9 Streamlines on the rotor, a. based on the time-averaged velocity, b. c. and d. based on the velocity at different mesh/rotor location. ($\mu = 0.243$)

The rotor blade experiences tip stall when the blade begins to retreat (Fig.9). This phenomenon does not appear in the time-averaged results but only instantaneously. Note that Fig. 9a represents the streamlines based on the time-averaged velocity. Figs. 9b-d show the streamlines based on the instantaneous velocity at several time steps (thus several rotor positions). Based on this result the stalled region is indicated in Fig. 9d. This region clearly depends on the advancing and retreating condition because of its asymmetric behavior. The tip stall experienced on the rotor blade is linked to the recirculation area provoked by the flow separation on the inlet. The stalled area as well as the recirculation bubble show an unsteady behavior due to the fan rotation. The pressure load on the rotor blades is also highly distorted and unsteady. This pressure

distribution modifies the fan characteristic point and considerably reduces its efficiency compared to an ideal inflow.

3.3.3 Cross-flow at the fan exit

The jet interaction with the cross-flow at the fan exit affects the fan efficiency. As seen before, the jet generated by the fan blocks the freestream and therefore increases the pressure in a region upstream of the jet nozzle (Fig. 10).

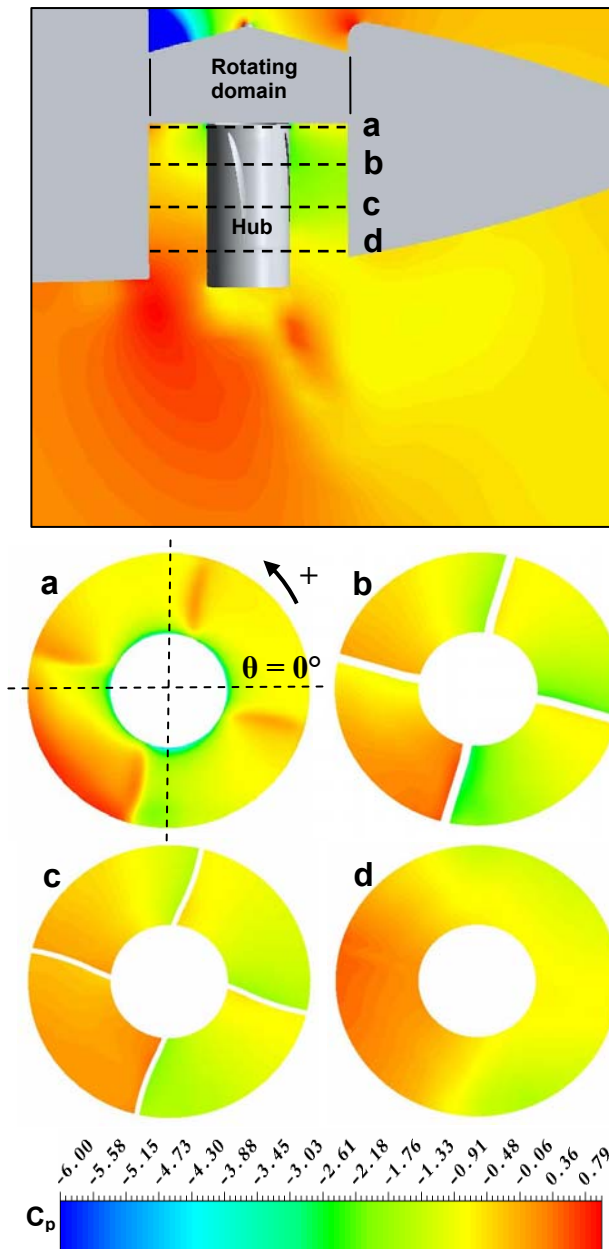


Fig. 10 C_p contour of internal sections, **a.** $-0.04 t$ **b.** $0.11 t$, **c.** $0.25 t$, **d.** $0.39 t$ in the transverse direction (t is the wing maximum thickness). $\alpha = 0^\circ$, $V_\infty = 40$ m/s, $N = 26,200$ rpm ($\mu = 0.243$)

A back pressure at the fan exit is present. The C_p -contours of the time-averaged pressure

coefficient in the stator surroundings confirm this last conclusion. The back-pressure at the exit can be seen in section c and d. Section a. is located right beneath the rotating domain. At this location, the non-uniform pressure distribution is caused mainly by the inflow distortion. As seen before, at $\theta = 180^\circ$, an area with high velocities and low pressure is created at the fan inflow.

The back-pressure generated by the cross-flow clearly affects the internal pressure distribution. Thus, the fan operating point is also affected by the back-pressure and consequently the fan efficiency is reduced. This conclusion is corroborated by the comparison of the thrust coefficient with the static thrust coefficient measured at zero airspeed in the wind tunnel. According to the time-averaged results the fan thrust coefficient, C_T is about 0.034. The static thrust coefficient is twice the dynamic one. The reduced fan performance is due to a combined effect of the inflow distortion and the back-pressure effect at the fan exit. Inlet guide vanes, outlet guide vanes and an inclination of the fan rotational axis could improve the fan performance by creating a more homogenous internal pressure distribution. All this confirms the fact that inflow distortion is one of the major issues for the efficiency of a fan-in-wing configuration.

3.3.4 Counter-rotating pair of vortices

As seen before in Fig. 7, the jet is swept back by the freestream and a backward flow is generated downstream of the fan exit on the lower side of the wing. The jet exiting the fan nozzle rolls up in a pair of counter-rotating vortices. The jet trajectory follows a curved path while its cross section increases (Fig. 11). The position of the wing is indicated by a dotted line. The maximum eddy viscosity level is reached at 1.3 c. At this location the counter-rotating pair of vortices exhibits a well formed “kidney shape”. The eddy-viscosity level decreases after reaching its maximum at 1.3 c and remains significant at several chords downstream of the nozzle. The pair of vortices clearly dominates the far field and has an important effect on the wing performance inducing considerable pressure drag and a lift loss on the wing part downstream of the nozzle. This is confirmed by

the chordwise pressure distribution shown in the next section (Fig. 12). In the far field, at $x/c = 3$ the slip wall boundary condition, located on the right side of the picture, affects the vortex shape and reduces its strength. x, y, z are the streamwise, spanwise and transverse coordinate directions respectively. The coordinate system origin is the wing leading edge

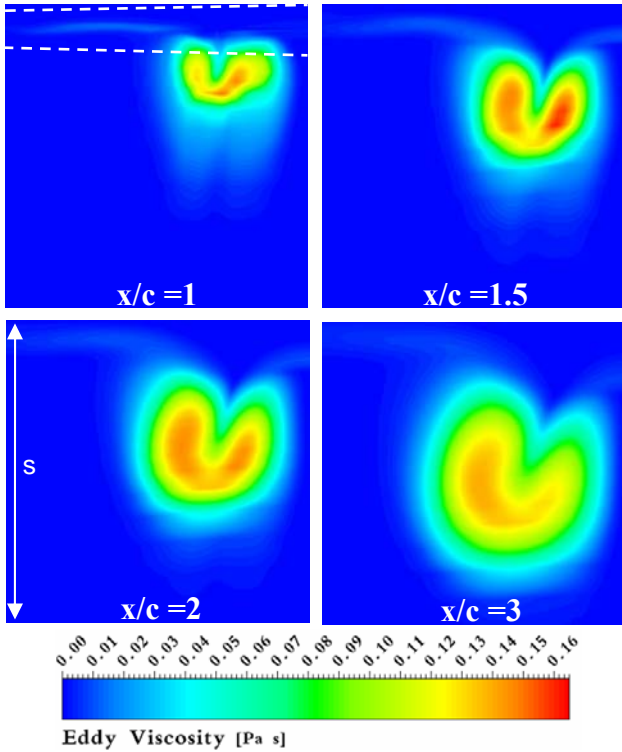


Fig. 11 Eddy-viscosity at different streamwise locations ($\alpha = 0^\circ$, $V_\infty = 40$ m/s, $N = 26,200$ rpm, $\mu = 0.243$).

4 Comparison of numerical and exp. data

In this section, a comparison of the experimental data with the time-averaged URANS results is made.

4.1 Forces

The overall drag coefficient predicted by the code shows a very good agreement with the experimental data (Table 3). The lift coefficient, C_L , exhibits a good prediction by the simulation. The relative difference in lift coefficient is less significant at $\alpha = 0^\circ$ than at $\alpha = 5^\circ$. As shown, the airfoil asymmetry affects the lift and pitching moment coefficient at high angle of attack. According to section 2, the jet flap effect created by the jet enhances the circulation

around the wing. Therefore, the effects induced by the geometrical imperfection are more significant than for the corresponding case without fan for a given α . The pitching moment, with respect to the quarter chord is predicted quantitatively correctly. Considering the small values of C_m , the relative difference is not relevant.

	CFD	EXP	Relative difference
C_L	0.272	0.298	8.7%
	0.483	0.403	16.6%
C_D	0.097	0.101	4.0%
	0.120	0.123	2.4%
C_m	-0.038	-0.055	-
	-0.027	-0.007	-

Table 3 Force measurements comparison: **upper line**, $\alpha = 0^\circ$, $V_\infty = 40$ m/s, $N = 26,200$ rpm; **lower line** $\alpha = 5^\circ$, $V_\infty = 30$ m/s, $N = 21,000$ rpm.

4.2 Pressure distribution

Two chordwise pressure distributions located in the spanwise direction at $1/3 s$ and $2/3 s$ are investigated. The suction peak on the rear part downstream of the jet, due to the jet mixing with the cross flow, shows a good agreement with the experimental measurements (Fig. 12b). The overall pressure distribution shows a good agreement with the experiment for both chordwise distributions (Fig. 12a). The profile asymmetry is responsible for the difference at the leading and trailing edge. This has been confirmed by the chordwise pressure distribution analysis on the wing without fans. Radial pressure distribution around the inlet radius and nozzle, not presented in this paper, show also a good agreement with the experimental data. Note that small pressure oscillations can be observed roughly between 65% and 75% of the chord. This is due to an insufficient refinement in the spanwise direction far from the inlet radius. This effect is negligible.

4.3 Surface streamlines

Wool-tufts flow visualization provides an overview of the wing surface streamlines. In the simulation, the streamlines are based on the time-averaged velocity. The reattachment of the

boundary layer on the wing upper side and downstream of the fan can be seen on both numerical and experimental results (Fig. 13).

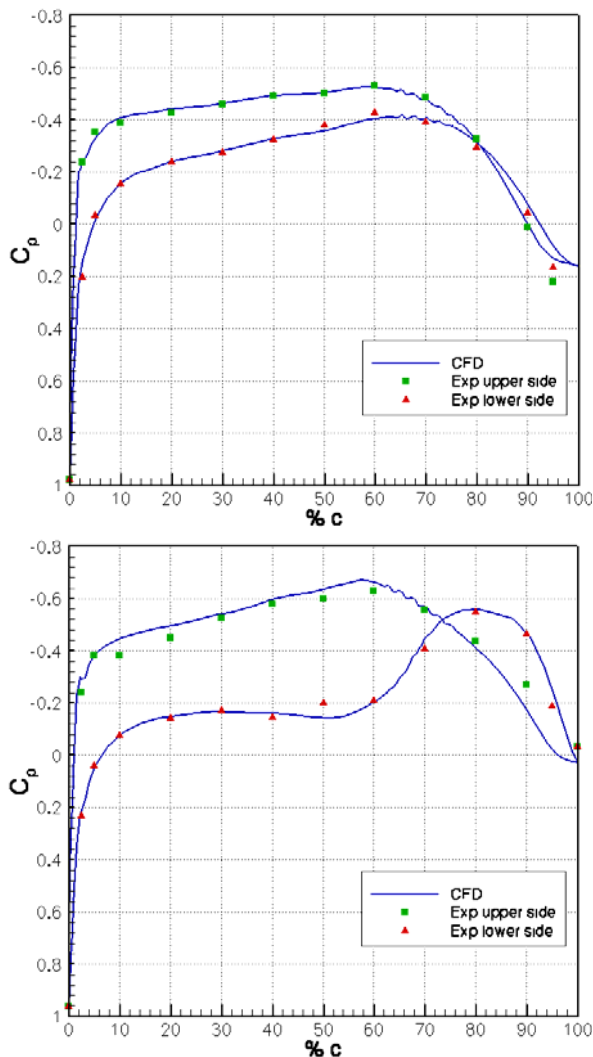


Fig. 12 Chordwise pressure distribution comparison, a. at 2/3 s and b. at 1/3 s from the wing root chord ($\alpha = 0^\circ$, $V_\infty = 40$ m/s, $N = 26,200$ rpm, ($\mu = 0.243$)).

The separation at the trailing edge over this area is also relatively well described by the CFD at $\alpha = 0^\circ$. The small separation area on the experimental picture, however, is not reproduced by the code. This small area (circled in red) occurs in a low momentum region where streamlines are ingested. This effect is linked to the retreating and advancing condition on the rotor blades identified in section 3. On the wing lower side, the overall shape of the suction area appears to be well captured by the code. The horseshoe vortex, clearly visible numerically, matches with the experimental picture. The separation occurring at the trailing edge and

over the fan is also well described by the simulation at zero angle of incidence.

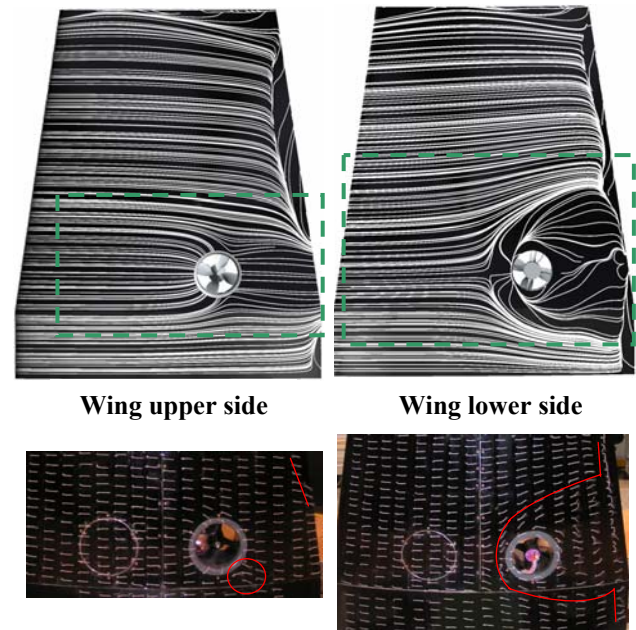


Fig. 13 Streamlines visualization comparison at $\alpha = 0^\circ$, $V_\infty = 40$ m/s, $N = 26,200$ rpm ($\mu = 0.243$).

4.4 PIV

Flow field mapping based on PIV measurements provide quantitative velocity data for comparison downstream of the fan exit.

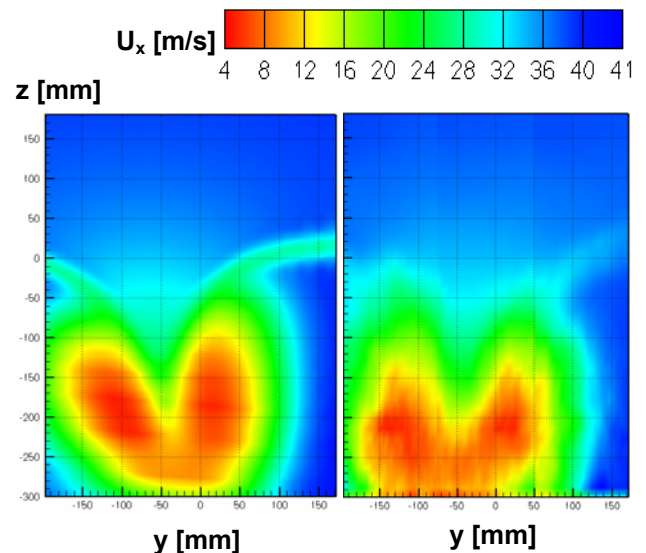


Fig. 14 Streamwise velocity component, U_x , in a cross flow plane located at 1.22 c. **left:** CFD results, **right:** experimental results. The picture center ($y = 0$ mm and $z = 0$ mm) is located at $x = 1.22$ c, $y = 0.18$ s, and $z = -0.14$ t. $\alpha = 0^\circ$, $V_\infty = 40$ m/s, $N = 26,200$ rpm ($\mu = 0.243$)

The PIV measurement has been performed at 1.22 c downstream of the fan to capture the pair of counter-rotating vortices. The “kidney shape” as well as the location of the velocity contours is well predicted by the numerical simulation (Fig.14). For the closed wing without fan, the trailing edge wake is located at the line $z = 0$ at $\alpha = 0^\circ$. For the fan-in-wing configuration, the trailing edge wake can be seen in regions below ($z = 0$ mm, $y = -150$ mm) and above ($z = 0$ mm, $y = -100$ mm). The position of the trailing edge wake is well described by the simulation. The velocity magnitude and the position of the vortex core are also in agreement with the experimental results. PIV results performed at 1.1 c, not presented here, corroborates the last conclusions.

5 Conclusion and outlook

URANS simulations using the ANSYS CFX flow simulation software were conducted for a fan-in-wing configuration using a sliding mesh technique. A block-structured mesh of the entire geometry was performed. Time-averaged results over one fan revolution were discussed for selected operating conditions and compared to experimental data. A wide range of experimental techniques including force measurements, surface static pressure measurements, PIV and wool tufts visualization was used to proof the numerical results. A small geometrical difference between the wind tunnel model and the computed geometry has been detected and induce a different airfoil behavior especially at high angle of attack.

The unsteady behavior of a recirculation area above the rotor blades due to the separation on the fan inlet was analyzed. The back-pressure in the internal flow due to the jet blockage upstream of the nozzle was studied. The main features encountered in a jet-in-cross-flow are a horseshoe vortex on the wing lower side, wake vortices, and generation and spreading of a counter-rotating vortex. These characteristics are predicted by the simulation for all investigated angles of attack and tip-speed ratios. Despite a small asymmetry in the wind tunnel model airfoil, a good agreement was observed between the numerical results and the

whole range of experimental data including PIV, forces, surface pressures and streamlines for moderate angle of attack.

Further analysis will be carried out on the flow topology and calculation using a multiblock solver will be undertaken.

Acknowledgments

The authors would like to thank ANSYS CFX for providing the flow simulation software. This study was funded by the Bauhaus Luftfahrt e. V.

References

- [1] Diedrich J. H., NASA TM X-71778, Summary of model VTOL lift fan tests conducted at NASA Lewis research center, 1975
- [2] Hickey D. H., Kirk J. V., NASA CR-177615, Survey of Lift-Fan Aerodynamic Technology NASA Ames center, 1993
- [3] Saddington A.J., Knowles K. A review of out-of-ground-effect propulsion-induced interference on STOVL aircraft. Progress in Aerospace Sciences Vol. 41, pp 175-191, 2005.
- [4] Kelso, R. M., and Smits, A. J., Horseshoe vortex systems resulting from the interaction between the laminar boundary layer and a transverse jet, Physics of Fluids, Vol. 7, pp. 153-158, 1995
- [5] Kelso, R. M., Lim, T. T., and Perry, A. E., An experimental study of round jets in cross-flow, Journal of fluid Mechanics, Vol. 306, pp. 111-114, 1996
- [6] Fric, T. F., and Roshko, A., Vortical structure in the wake of a transverse jet, Journal of Fluid Mechanics, Vol. 279, pp. 1-47, 1994
- [7] Cortelezzi, L. Karagozian, A. R., On the formation of the counter-rotating vortex pair in transverse jets, Journal of Fluid Mechanics, Vol. 446, pp. 347-373, 2001
- [8] Kummer J.D., Dang T. Q., High-Lift Propulsive Airfoil Integrated Crossflow Fan, Journal of Aircraft, Vol. 43, No. 4, pp 1059-1069, 2006.
- [9] Thouault et al., Experimental investigations on generic fan-in-wing configurations, Proceedings of the International Powered Lift Conference, July 22-24 2008, London
- [10] Hickey D. H., Ellis D. R., Wind-Tunnel tests of a semispan wing with a fan rotating in the plane of the wing, NASA TN D-88, 1959
- [11] Menter F. R., Two equations eddy viscosity turbulence models for engineering applications, AIAA journal, Vol. 32, pp. 1598-1605, 1994
- [12] GGI and MFR, ANSYS CFX 11 user's guide.

Copyright Statement

The authors confirm that they, and/or their company or institution, hold copyright on all of the original material included in their paper. They also confirm they have obtained permission, from the copyright holder of any third party material included in their paper, to publish it as part of their paper. The authors grant full permission for the publication and distribution of their paper as part of the ICAS2008 proceedings or as individual off-prints from the proceedings.